13. P. Guyon *et al.*, *Atmos. Chem. Phys.* **3**, 951 (2003).
14. G. Roberts, P. Artaxo, J. Zhou, E. Swietlicki, M. O. Andreae, *J. Geophys. Res.* **107**, 10.1029/2001JD000583 (2002).
15. G. C. Roberts, A. Nenes, J. H. Seinfeld, M. O. Andreae, *J. Geophys. Res.* **108**, 10.1029/2001JD000985 (2003).
16. D. Rosenfeld, R. Lahav, A. Khain, M. Pinsky, *Science* **297**, 1667 (2002).
17. M. O. Andreae, S. J. de Mora, W. Elbert, *J. Geophys. Res.* **100**, 11335 (1995).
18. L. F. Radke *et al.*, in *Global Biomass Burning: Atmospheric, Climatic and Biospheric Implications*, J. S. Levine, Ed. (MIT Press, Cambridge, MA, 1991), pp. 209–224.
19. M. O. Andreae *et al.*, in preparation.
20. D. Rosenfeld, I. M. Lensky, *Bull. Am. Meteorol. Soc.* **79**, 2457 (1998).
21. D. Rosenfeld *et al.*, paper presented at the Seventh World Meteorological Organization Scientific Conference on Weather Modification, Chiang Mai, Thailand, 17 to 22 February 1999.
22. MODIS (Moderate Resolution Imaging Spectrometer) onboard NASA's AQUA satellite, passing over around 13:30 solar time.
23. B. Graham *et al.*, *J. Geophys. Res.* **107**, 10.1029/2001JD000336 (2002).
24. O. L. Mayol-Bracero *et al.*, *J. Geophys. Res.* **107**, 10.1029/2001JD000522 (2002).
25. R. J. Ferek, J. S. Reid, P. V. Hobbs, D. R. Blake, C. Liousse, *J. Geophys. Res.* **103**, 32107 (1998).
26. J. S. Reid *et al.*, *J. Geophys. Res.* **103**, 32,059 (1998).
27. J. S. Reid, P. V. Hobbs, A. L. Rangno, D. A. Hegg, *J. Geophys. Res.* **104**, 6145 (1999).
28. A. S. Procopio, L. A. Remer, P. Artaxo, Y. J. Kaufman, B. N. Holben, *Geophys. Res. Lett.* 2003GL018063RR (2003).
29. J. Molinié, C. A. Pontikis, *Geophys. Res. Lett.* **22**, 1085 (1995).
30. E. J. Zipser, *Mon. Weather Rev.* **122**, 1837 (1994).
31. F. J. Nober, H.-F. Graf, D. Rosenfeld, *Global Planet. Change* **37**, 57 (2003).
32. A. Kasahara, P. L. D. Dias, *J. Atmos. Sci.* **43**, 1893 (1986).
33. A. M. Grimm, P. L. D. Dias, *J. Atmos. Sci.* **52**, 3538 (1995).
34. P. V. Hobbs *et al.*, *J. Geophys. Res.* **108**, 10.1029/2002JD002352 (2003).
35. M. O. Andreae *et al.*, *Geophys. Res. Lett.* **28**, 951 (2001).
36. S. Sherwood, *Science* **295**, 1272 (2002).
37. M. B. Baker, R. J. Charlson, *Nature* **345**, 142 (1990).
38. S. R. Freitas, M. A. F. Silva Dias, P. L. Silva Dias, *Hybrid Methods Eng.* **2**, 317 (2000).

39. We thank all members of the LBA-SMOCC–Cooperative LBA Airborne Experiment 2002 and LBA–Radiation, Cloud, and Climate Interactions science teams for their support during the field campaign, especially J. von Jouanne, M. Welling, P. Guyon, G. Nishioka, T. Germano, and the pilots of the Universidad Estadual do Ceará (UECE) and Instituto Nacional do Pesquisas Espaciais (INPE) aircraft. We thank E. Freud for help with the scientific processing of the cloud physics aircraft data, M. Lawrence for providing results from the MATCH model, and E. Williams for stimulating discussions about the manuscript. This project was funded by the European Commission (Project SMOCC), the Max Planck Society, the Fundação de Amparo à Pesquisa do Estado de São Paulo, and the Conselho Nacional de Desenvolvimento Científico (Instituto do Milênio LBA).

Supporting Online Material

www.sciencemag.org/cgi/content/full/303/5662/1337/DC1
Materials and Methods
Figs. S1 to S10
References and Notes

11 December 2003; accepted 23 January 2004

REPORTS

Measurement of the Effect of Amazon Smoke on Inhibition of Cloud Formation

Ilan Koren,[1,2]* Yoram J. Kaufman,[1] Lorraine A. Remer,[1] Jose V. Martins[1,3]

Urban air pollution and smoke from fires have been modeled to reduce cloud formation by absorbing sunlight, thereby cooling the surface and heating the atmosphere. Satellite data over the Amazon region during the biomass burning season showed that scattered cumulus cloud cover was reduced from 38% in clean conditions to 0% for heavy smoke (optical depth of 1.3). This response to the smoke radiative effect reverses the regional smoke instantaneous forcing of climate from –28 watts per square meter in cloud-free conditions to +8 watts per square meter once the reduction of cloud cover is accounted for.

The net effect of aerosols on the atmospheric radiation budget and climate constitutes the greatest uncertainty in attempts to model and predict climate (*1*). Aerosols can counteract regional greenhouse warming by reflecting solar radiation to space or by enhancing cloud reflectance (*2*) or lifetime (*3*, *4*). However, aerosol absorption of sunlight is hypothesized to slow down the hydrological cycle and influence climate in ways not matched by the greenhouse effects (*5*, *6*). During periods of heavy aerosol concentration over the Indian Ocean (*7*) and Amazon basin (*8*), for example, measurements have revealed that absorbing aerosols warmed the lowest 2 to 4 km of the atmosphere while reducing by 15% the amount of sunlight reaching the surface.

Less irradiation of the surface means less evaporation from vegetation and water bodies, and (unless the smoke is concentrated near the surface only) a more stable and drier atmosphere, and consequently less cloud formation. This effect was defined theoretically as a positive feedback to aerosol absorption of sunlight (*9*) and was termed the semi-direct effect. A similar process, defined as cloud burning by soot, in which solar heating by the aerosol reaches its maximum near the top of the boundary layer, thereby stabilizing the boundary layer and suppressing convection, has been described (*10*). These cloud simulations were based on aerosol observations of INDOEX (Indian Ocean Experiment) (*11*) and focused mainly on the amplification of daytime clearing due to aerosol heating. Reduction of evaporation from the Mediterranean Sea by pollution from northern and eastern Europe was modeled to reduce cloud formation and precipitation over the Mediterranean region (*12*), in general agreement with measurements (*13*). However, warming of the atmosphere by similar widespread pollution aerosol over southeastern China was modeled to cause uplift of the polluted air mass over an area of 10 million km^2, which then was replaced by cooler moist air from the nearby Pacific Ocean, causing an increase in precipitation and flooding that fits observations from this region in recent years (*14*).

Here, using data from the MODIS-Aqua space instrument, we report measurements of the effect of smoke on cloud formation over the Amazon basin during the dry season (August–September) of 2002—namely, the reduction of the fraction of scattered cumulus clouds with the increase in smoke column concentration.

The area is under the influence of a regional high-pressure zone above a surface boundary layer and is associated with lower precipitation, land clearing, and biomass burning. The moisture source for the cloud formation and precipitation in the region is water vapor evaporated locally through plant evapotranspiration and moisture transported from the Atlantic Ocean (*15*), each responsible for half of the moisture that falls as precipitation. Easterly winds carry the moisture from the Atlantic Ocean throughout the Amazon basin until they reach the barrier of the Andes, where they decrease in velocity and veer either north or south (*16*) (Fig. 1).

The scattered cumulus clouds (also called boundary layer clouds) emerge regularly in the morning over the eastern shore. By local

[1]NASA Goddard Space Flight Center (GSFC), Greenbelt, MD 20771, USA. [2]National Research Council, Washington, DC 20001, USA. [3]Joint Center for Earth Systems Technology, University of Maryland, Baltimore County, Baltimore, MD 21250, USA.

*To whom correspondence should be addressed. E-mail: ilank@climate.gsfc.nasa.gov

noon they cover large parts of the Amazon basin. The cloud diameter is on average 2 to 3 km, with average reflectance of 0.35 in the visible part of the solar spectrum. The clouds are sensitive to the surface properties and seldom form directly above the Amazon River. The stable meteorological conditions and the regular behavior of the clouds in the absence of smoke create an ideal case to study the impact of aerosol from biomass burning on cloud formation. Satellite images of the absence of clouds in smoky regions and differences between morning and afternoon are shown in Fig. 2. In the afternoon, clouds uniformly cover the region of the Amazon forest that is not filled with high concentrations of smoke.

To estimate the effect of smoke on cloud coverage and the "semi-direct" forcing on climate, we measured the cloud fraction as a function of the smoke optical depth (OD) in the cloud vicinity (*17*). To isolate the effect of smoke on cloud fraction, it is necessary to minimize any residual influences of synoptic conditions (wind, humidity) and variation of surface cover. Therefore, the following restrictions on the satellite data were used in the analysis: (i) Data are analyzed only from the MODIS-Aqua platform at 13:30 local time (±15 min) over the Amazon basin, when the scattered cumulus fields are well developed and cover more then 85% of the forest. (ii) The area of interest was restricted to the Amazon basin between 8°N and 12°S and between 44° and 76°W, but only with forest background coverage. (iii) For comparison we analyzed the western part of the area (Andes to Manaus on the east) separately from the eastern part (the low Amazon, Manaus to the east coast). (iv) Wind field maps of the area at three different pressure levels (near ground, 925 mbar, 850 mbar, and 700 mbar) at 14:00 local time [NOAA National Centers for Environmental Prediction (*18*)] were used to filter out cases with nonstandard wind flow patterns. Of 200 Aqua images, 50 granules, with minimum area of ~20,000 km^2 each, met the above restrictions and were analyzed.

Clouds were detected and separated from smoke by their high local spatial variability and brightness reflectance (*19*). Size and spatial variability were then used to classify between the small scattered cumulus and other types of clouds. The smoke ODs were calculated by the MODIS (*20*) algorithm in the noncloudy area.

The spatially smooth OD field was divided into 100 steps and used to generate a histogram of cloud fraction (Fig. 3). The cloud fraction decreases continuously as a function of smoke OD. The small differences between the eastern and western regions may result from the differences in the average elevation, distance from the ocean, and weaker winds in the west. The eastern and western regions show similar results. On average, the cloud fraction decreases by 50% for OD = 0.6.

What is the effect of the reduction in cloud cover on the regional energy balance? To estimate the semi-direct effect on the climate forcing, we used the one-dimensional radiation transfer model (*21*, *22*) to model the spectrally integrated radiative flux divergence in the smoky atmosphere. The inputs for the model were profiles of temperature, humidity, atmospheric gases, clouds, and aerosol in the tropical atmosphere. The cloud

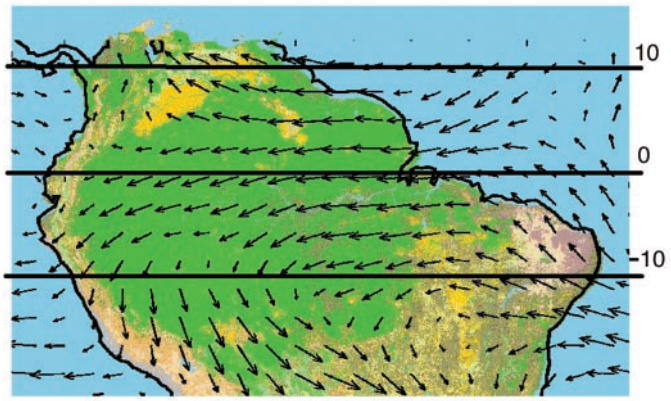

Fig. 1. A wind map (pressure level, 850 mbar) superimposed on a corresponding map showing the extent of the Amazon rainforest in green.

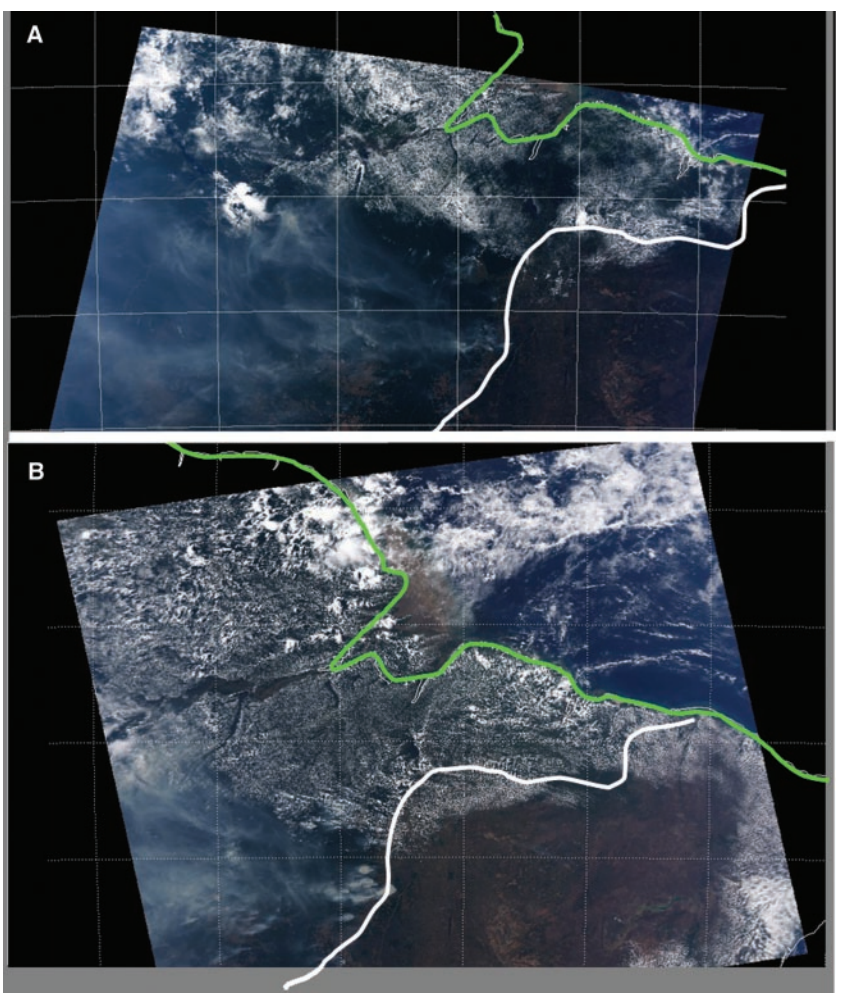

Fig. 2. Terra and Aqua satellite images of the east Amazon basin, 11 August 2002. (**A**) The clouds (Terra, 10:00 local time) are beginning to form. (**B**) The clouds (Aqua, 13:00 local time) are fully developed and cover the whole Amazon forest except for the smoke area. The boundary between forest and Cerrado region is marked in white on both images, and the seashore is marked in green. Note that the Amazon River and tributaries are a cloud-free area.

properties were taken from MODIS cloud measurements with average optical depth of 8, and elevation of 760 mbar (~2.3 km), situated above the smoke layer.

The modeled results for the warming effect of smoke absorption with and without clouds are shown in Fig. 4. Without clouds, the heating of the layer (°C/day) increases monotonically with the smoke OD, with maximum heating occurring at the top of the smoke layer. In the presence of a mix of smoke and clouds according to the proportions in Fig. 3, the strong longwave cooling at the top of the clouds is gradually replaced by warming of the smoke layer as the OD grows and the clouds are eliminated. As the smoke layer becomes warmer (relative to the surface) as a result of the smoke absorption and scattering, the whole layer between top of the smoke and surface becomes more stable.

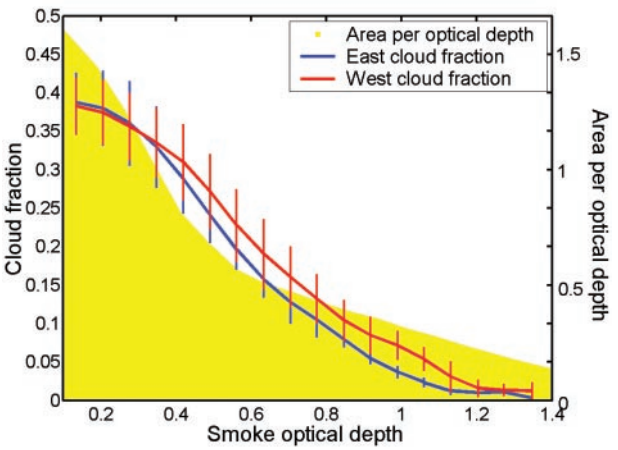

Fig. 3. Cloud fraction as function of aerosol optical depth (OD), a measure of the extinction of a beam of light when it passes through a column of atmosphere. The cloud fraction decreases almost linearly with increasing OD. The red and blue curves denote the average of 23 granules in the east and 27 granules in the west of the Amazon, respectively. The estimated error for each point appears as error bars. On average, the cloud fraction decreases to less than 1/8 of the cloud fraction in clean conditions when OD = 1. The differences between western and eastern areas may be due to differences in local conditions (altitude, wind velocity). The shaded area represents the relative area covered by the respective OD, with the integral of this curve equal to 1, representing the total Amazon basin.

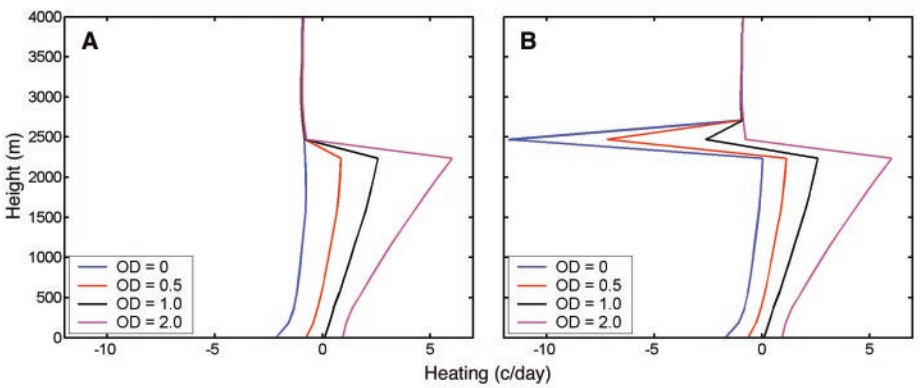

Fig. 4. Heating profiles for smoke optical depth of 0, 0.5, 1.0, and 2.0. Smoke single scattering albedo is 0.91. (**A**) Smoke only with no clouds. (**B**) Smoke with cloud fraction as found in analysis of Aqua observations.

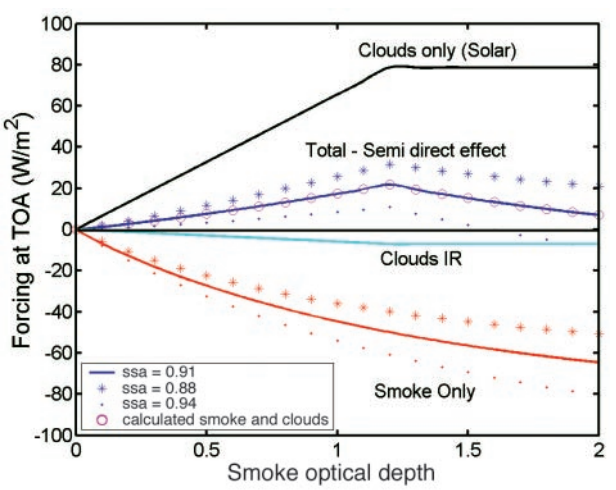

Fig. 5. Radiative forcing at the top of the atmosphere as a function of the smoke optical depth. The slope breaks near optical depth = 1.3 when the cloud fraction approaches zero. The black, red, and light blue lines represent the forcing in the solar spectrum (shortwave) due to the reduction in the cloud cover, the smoke negative forcing, and longwave radiative cooling, respectively. The combined radiative effect is shown by the dark blue curve. The magenta circles are a reproduction of the combined smoke and cloud effect using a weighted combination of the black and red curves (with the use of Eq. 1).

Next, we calculated the radiative forcing at the top of the atmosphere (TOA). Radiative forcing is defined as the change in the radiation balance with and without the forcing element (*1*). In this study the forcing element is the radiative effect of the smoke and of the reduction in the cloud cover. Radiative forcing is, in this case, the difference in the reflected radiative flux at TOA between the background conditions (OD = 0.1) and a given value of OD. A negative forcing at TOA corresponds to cooling of Earth's atmosphere and surface system, and positive forcing corresponds to warming. The black line in Fig. 5 represents the forcing in the solar spectrum (shortwave) due to the reduction in the cloud cover, from 38% for background aerosol to almost zero at OD of 1.3. Reduction in the cloud coverage reduces the reflection of the solar flux at TOA—a positive forcing. Smoke reflectance (red curve) generates negative forcing. As the cloud fraction decreases, the infrared (IR) trapping by the clouds decreases, resulting in a longwave radiative cooling effect (light blue curve). The overall cooling effect of the longwave part of the spectrum is less than 10% of the warming in the shortwave part.

The combined radiative effect of clouds and smoke in the solar and IR parts of the spectrum is shown by the dark blue curve in Fig. 5. The dominant forcing for OD < 1.3 is the reduction in the cloud fraction, partly balanced by the increase in the smoke reflectance. Above this OD there are no clouds left and the only forcing is due to smoke, causing a reversal in the trend of the forcing. The total forcing F_t can be expressed as

$$F_t = (F_{cs} + F_{cir}) \cdot cf + F_s \cdot (1 - cf) + (F_s \cdot cf \cdot tr_c^2) \quad (1)$$

where F_{cs} is the cloud forcing in the solar part of the spectrum, F_{cir} is the cloud forcing in the IR, cf is the cloud fraction (hence $1 - cf$ is the cloud-free area), and F_s is the contribution of the smoke forcing. The last term is the contribution of transmission of the smoke forcing through the clouds on a two-way path (tr_c^2).

The overall radiative forcing of the semi-direct effect in the area is the integral of the combined forcing, F_t, on OD, weighted by the occurrence of that OD from Fig. 3. The estimated instantaneous forcing for aerosol single scattering albedo (SSA) of 0.91 (meaning that 9% of the aerosol interaction with

light results in absorption) (*23*) is 8 W/m^2, composed of smoke negative forcing of –28 W/m^2 and cloud reduction positive forcing of +22 W/m^2. The sensitivity of the forcing to the value of SSA is linear. For SSA = 0.88, the forcing increases to 13 W/m^2; for SSA = 0.94, the forcing decreases to 3 W/m^2.

The 24-hour average forcing is estimated on the basis of observations (Fig. 1) that the lifetime of the boundary layer cloud fields is 4 ± 2 afternoon hours, shorter than the duration of the smoke (10 ± 2 hours). Therefore, the 24-hour average of combined clouds and smoke forcing is –5.5 ± 2 W/m^2, instead of forcing of smoke only of –11.5 ± 2 W/m^2. Inclusion of the smoke semi-direct effect reduces to less than half the 24-hour average forcing from previous estimates (*24*, *25*) and converts the instantaneous forcing in the afternoon to positive forcing (warming) rather than negative forcing (cooling) for the smoke alone.

The proposed mechanism for the smoke reduction of cloud fraction can be described as a combination of a few dependent feedback processes. The first is the direct aerosol effect on stabilizing the boundary layer by heating of the aerosol layer and cooling of the surface caused by the aerosol scattering and absorption (shading the surface from solar flux). This process by itself reduces the convectivity and boundary layer cloud formation. Second, reduction of solar flux reaching the canopy tends to decrease evapotranspiration and the moisture input to the atmosphere (*26*). The small amount of moisture released by evapotranspiration in smoky conditions remains near the canopy because of decreased turbulent fluxes within the boundary layer. Third, because of the heating of the aerosol layer by absorption, the capacity of the layer to hold water vapor increases and there is less likelihood to reach supersaturation and form clouds. The fourth process is the competition for water vapor by the extremely high concentrations of particles that share the condensed water and keep the layer from reaching supersaturation (*27*, *28*). Detailed descriptions of the aerosol effects and feedbacks are given in (*29*).

Analysis of satellite data has documented the relationship between heavy aerosol and the formation of scattered cumulus clouds. Possible effects on deeper convection have so far been ignored. Even though the smoke aerosol in the Amazon absorbs light one-tenth as much as it scatters light, the absorption is enough to heat the atmosphere by 2° to 4°C per day and to change the energy balance between the surface and the atmosphere in a way that stabilizes the boundary layer. However, for a neutral atmosphere, stabilizing one layer of the atmosphere destabilizes the layer above it. If the humidity can penetrate the inversion at the top of the smoke layer, then it will reach a very unstable layer, creating larger deep convective clouds (*30*). Such clouds can be observed sporadically in the satellite images, but with no correlation to the presence of the smoke. Our results show that smoke, instead of cooling the climate, warms it in the afternoon hours when the scattered cumulus clouds can form. The 24-hour forcing reduces the net forcing to –5.5 ± 2 W/m^2, less than half of net forcing from smoke alone. The reduction in cloud fraction by absorbing aerosol may be an important mechanism to explain why Earth warmed substantially in the last century despite the expected aerosol cooling effect.

References and Notes

1. Intergovernmental Panel on Climate Change, *Climate Change 2001—The Scientific Basis* (*Contribution of Working Group I to the Third Assessment Report of the Intergovernmental Panel on Climate Change*) (Cambridge Univ. Press, Cambridge, 2001).
2. S. Twomey, *J. Atmos. Sci.* **34**, 1149 (1977).
3. A. B. Albrecht, *Science* **245**, 1227 (1989).
4. D. Rosenfeld, *Science* **287**, 1793 (2000).
5. V. Ramanathan, P. J. Crutzen, J. T. Kiehl, D. Rosenfeld, *Science* **294**, 2119 (2001).
6. Y. J. Kaufman, D. Tanré, O. Boucher, *Nature* **419**, 215 (2002).
7. S. K. Satheesh, V. Ramanathan, *Nature* **405**, 60 (2000).
8. T. Eck, B. N. Holben, I. Slutsker, A. Setzer, *J. Geophys. Res.* **103**, 31865 (1998).
9. J. Hansen, M. Sato, R. Ruedy, *J. Geophys. Res.* **102**, 6831 (1997).
10. A. S. Ackerman *et al.*, *Science* **288**, 1042 (2000).
11. A. J. Heymsfield, G. M. McFarquhar, *J. Geophys. Res.* **106**, 28653 (2001).
12. J. Lelieveld *et al.*, *Science* **298**, 794 (2002).
13. P. Alpert *et al.*, *Geophys. Res. Lett.* **29** (11), 10.1029/2001GL013554 (2002).
14. S. Menon, J. Hansen, L. Nazarenko, Y. Luo, *Science* **297**, 2250 (2002).
15. E. Salati, in *The Forest and the Hydrological Cycle: Geophysiology of Amazonia*, R. E. Dickinson, Ed. (Wiley, New York, 1987), pp. 273–296.
16. C. A. Nobre, L. F. Mattos, C. P. Dereczynski, T. A. Tarasova, I. V. Trosnikov, *J. Geophys. Res.* **103**, 31809 (1988).
17. See supporting data on *Science* Online.
18. E. Kalnay *et al.*, *Bull. Am. Meteorol. Soc.* **77**, 437 (1996).
19. J. V. Martins *et al.*, *Geophys. Res. Lett.* **29** (12), 10.1029/2001GL013252 (2002).
20. Y. J. Kaufman *et al.*, *J. Geophys. Res.* **102**, 17051 (1997).
21. M.-D. Chou, *J. Atmos. Sci.* **49**, 762 (1992).
22. M.-D. Chou, D. P. Kratz, W. Ridgway, *J. Clim.* **4**, 424 (1991).
23. O. Dubovik *et al.*, *J. Atmos. Sci.* **59**, 590 (2002).
24. J. E. Penner, R. E. Dickinson, C. A. O'Neill, *Science* **256**, 1432 (1992).
25. P. V. Hobbs, J. S. Reid, R. A. Kotchenruther, R. J. Ferek, R. Weiss, *Science* **275**, 1776 (1997).
26. D. Cohan, J. Xu, M. H. Bergin, W. L. Chameides, *Global Biogeochem. Cycles* **16** (4), 10.1029/2001GB001441 (2002).
27. H. Yu, S. C. Liu, R. E. Dickinson, *J. Geophys. Res.* **107** (D12), 10.1029/2001JD000754 (2002).
28. G. Feingold, L. A. Remer, J. Ramaprasad, Y. J. Kaufman, *J. Geophys. Res.* **106**, 22907 (2002).
29. M. Z. Jacobson, *J. Geophys. Res.* **107** (D19), 10.1029/2001JD001376 (2002).
30. Y. Rudich, A. Sagi, D. Rosenfeld, *J. Geophys. Res.* **108**, 4478 (2003).

31. This research was performed while I.K. held a National Research Council Research Associateship Award at NASA/GSFC.

Supporting Online Material

www.sciencemag.org/cgi/content/full/303/5662/1342/DC1
SOM Text
Figs. S1 to S5
References

21 July 2003; accepted 5 January 2004

Laser Guide Star Adaptive Optics Imaging Polarimetry of Herbig Ae/Be Stars

Marshall D. Perrin,[1,2]* James R. Graham,[1,2] Paul Kalas,[1,2] James P. Lloyd,[2,3] Claire E. Max,[2,4] Donald T. Gavel,[2,5] Deanna M. Pennington,[2,4] Elinor L. Gates[2,6]

We have used laser guide star adaptive optics and a near-infrared dual-channel imaging polarimeter to observe light scattered in the circumstellar environment of Herbig Ae/Be stars on scales of 100 to 300 astronomical units. We revealed a strongly polarized, biconical nebula 10 arc seconds (6000 astronomical units) in diameter around the star LkHα 198 and also observed a polarized jet-like feature associated with the deeply embedded source LkHα 198-IR. The star LkHα 233 presents a narrow, unpolarized dark lane consistent with an optically thick circumstellar disk blocking our direct view of the star. These data show that the lower-mass T Tauri and intermediate mass Herbig Ae/Be stars share a common evolutionary sequence.

Diffraction-limited optical and infrared astronomy from the ground requires adaptive optics (AO) compensation to eliminate atmospheric wavefront disturbances. Bright stars may be used as wavefront references for this correction, but most astronomical targets lack nearby guide stars. AO observations of these targets from the ground can only be accomplished with the use of artificial laser guide stars (LGS) (*1*).

Herbig Ae/Be stars are young stars with masses between 1.5 and 10 times that of the sun; they are the intermediate-mass counter-